Mechanical constraints on inversion of coseismic geodetic data for fault slip and geometry: Example from InSAR observation of the 6 October 2008 M_w 6.3 Dangxiong-Yangyi (Tibet) earthquake

Jianbao Sun,[1] Kaj M. Johnson,[2] Zhongquan Cao,[3] Zhengkang Shen,[1,4] Roland Bürgmann,[5] and Xiwei Xu[6]

[1]   Modern geodetic techniques, such as the global positioning system (GPS) and Interferometric Synthetic Aperture Radar (InSAR), provide high-precision deformation measurements of earthquakes. Through elastic models and mathematical optimization methods, the observations can be related to a slip distribution model. The classic linear, kinematic, and static slip inversion problem requires specification of a smoothing norm of slip parameters and a residual norm of the data and a choice about the relative weight between the two norms. Inversions for unknown fault geometry are nonlinear and, therefore, the fault geometry is often assumed to be known for the slip inversion problem. We present a new method to invert simultaneously for fault slip and fault geometry assuming a uniform stress drop over the slipping area of the fault. The method uses a full Bayesian inference method as an engine to estimate the posterior probability distribution of stress drop, fault geometry parameters, and fault slip. We validate the method with a synthetic data set and apply the method to InSAR observations of a moderate-sized normal faulting event, the 6 October 2008 M_w 6.3 Dangxiong-Yangyi (Tibet) earthquake. The results show a 45.0 ± 0.2° west dipping fault with a maximum net slip of ~1.13 m, and the static stress drop and rake angle are estimated as ~5.43 MPa and ~92.5°, respectively. The stress drop estimate falls within the typical range of earthquake stress drops known from previous studies.

1.   Introduction

[2]   Using the widely adopted solution of dislocation in an elastic half-space, coseismic surface displacements obtained from geodetic data can be used to infer fault geometry and spatial distribution of coseismic slip. Currently, three classes of inversion algorithms are often used to infer fault geometry and slip distribution using surface deformation observations: (1) A two-step procedure involving nonlinear optimization of fault geometry assuming uniform slip on a rectangular dis-location in an elastic half-space, followed by a standard kinematic inversion for the spatial distribution of slip on the fault with optimized geometry [*Árnadóttir and Segall*, 1994; *Jonsson et al.*, 2002; *Talebian et al.*, 2004]. (2) A mixed linear/nonlinear optimization scheme in which one iteratively searches for a best fitting solution by performing many linear slip inversions while varying fault geometry [*Fialko*, 2004; *Fukahata and Wright*, 2008; *Shen et al.*, 2009]. (3) Full nonlinear inversions for the joint posterior probability distributions of fault geometry parameters and slip on the fault [e.g., *Fukuda and Johnson*, 2008]. The first method simplifies the problem by separating the inversion into a nonlinear optimization problem followed by a linear slip distribution inversion. The second approach mixes the linear inversion with the nonlinear geometry inversion. Typically one uses a global optimization method, such as a simulated annealing algorithm, or a genetic algorithm, to find the best fitting fault geometry and a nonnegative least squares (NNLS) algorithm to invert for the slip distribution. The "probabilistic class" of inversion strategies involves sampling the complete posterior probability density function of all

[1]State Key Laboratory of Earthquake Dynamics, Institute of Geology, China Earthquake Administration, Beijing, China.
[2]Department of Geological Sciences, Indiana University, Bloomington, Indiana, USA.
[3]Xizang Seismological Bureau, Lhasa, China.
[4]Department of Geophysics, Peking University, Beijing, China.
[5]Department of Earth and Planetary Science, University of California, Berkeley, California, USA.
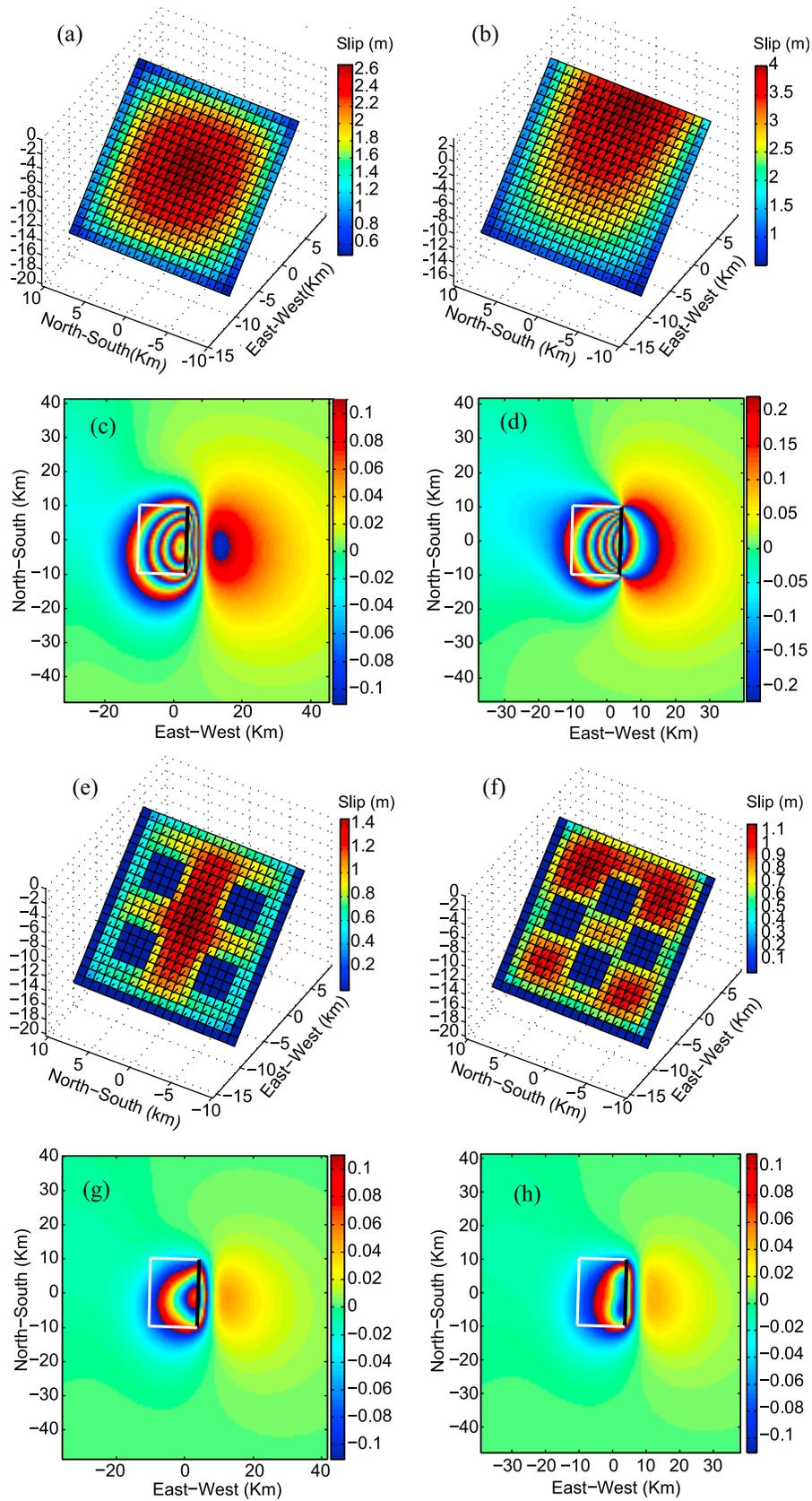[6]Institute of Geology, China Earthquake Administration, Beijing, China.

Figure 1

linear and nonlinear model parameters [*Fukuda and Johnson*, 2008]. All of the inversion algorithms discussed here could be referred to as "kinematic inversions" because the slip and geometry are inferred without regard for the mechanical relationship between slip and stress.

[3] It is well known that kinematic slip inversions require regularization to avoid unrealistically rough or oscillatory slip distributions. A smoothing constraint is introduced as prior information in the inversion [*Du et al.*, 1992; *Harris and Segall*, 1987]. The most common regularization approach in kinematic slip inversions is to minimize the norm of the residuals between the data and the model and some other smoothing norm of the slip distribution. A smoothing factor must be introduced that places the relative weight on minimizing the two norms. The smoothing factor is often selected from a trade-off curve between the misfit norm and a measure of smoothness or by objective methods including cross validation [*Matthews and Segall*, 1993] and Akaike's Bayesian information criterion (ABIC) [e.g., *Yabuki and Matsu'ura*, 1992]. *Fukuda and Johnson* [2008] recently developed a method for objectively determining the smoothing factor by the fully Bayesian inversion.

[4] This paper is concerned with the third class of slip inversions mentioned in the previous paragraph: full non-linear inversion for the joint posterior probability distribution of fault geometry parameters and slip on the fault. The fully Bayesian method of *Fukuda and Johnson* [2008] can, in principal, solve simultaneously for distributions of slip and unknown fault geometry parameters. However, the method is inefficient for the joint inversion because each slip patch is treated as an unknown parameter and the slip on all patches covaries strongly with geometry parameters. *Fukuda and Johnson* [2010] devised a mixed linear/non-linear Bayesian inverse formulation that can be used for the joint slip/geometry inversion, however this method requires that the relationship between slip and observations is linear, which precludes the use of positivity constraints. The ABIC method of *Fukahata and Wright* [2008] solves jointly for fault slip and fault dip angle, but the ABIC method cannot be applied with positivity constraints, as pointed out by *Fukuda and Johnson* [2008].

[5] In this paper, we introduce a new strategy for the slip inversion problem that can handle the joint slip/geometry inversion. In this inversion we assume that slip occurs under the condition of uniform shear stress drop on the fault plane and relate fault slip with the shear stress drop by a stress Green's function. The inversion does not require the specification of a smoothing norm and smoothing parameter and does not require the use of nonlinear least squares. As dis-

cussed below, the formulation of the inverse problem in terms of a uniform stress drop greatly reduces the size the model space compared with previous joint slip/geometry inversions.

[6] If the fault slip distribution is already known, the static stress drop can be computed by discretizing the slip into small patches and determining the stress change on the patches using the elastic dislocation solution of *Okada* [1992] or the fast wave number domain solution [*Ripperger and Mai*, 2004]. However, if we consider the shear stress change as being the unknown and estimating this in an inversion, the slip distribution can then be computed from the stress drop. In reality, the stress drop may be heterogeneously distributed on the fault plane. However, several studies suggest that the average stress drops computed globally are fairly uniform, varying over 2 orders of magnitude and the mean stress drop of 3.0 MPa is independent of earthquake size [e.g., *Allmann and Shearer*, 2009; *Hanks*, 1977; *Shaw*, 2009].

[7] We refer to our uniform stress drop inversion as a "mechanical" slip inversion to distinguish from the kinematic slip inversions that do not take the relationship between stress and slip on the fault into consideration. There are three main advantages to this mechanical slip inversion method. First, because the stress drop is assumed to be uniform, the slip distribution is inherently smooth. A smoothing norm and smoothing factor need not be introduced. Second, nonnegative constraints that are typically adopted for kinematic slip inversions are not needed because only moderate variations in rake of the slip vectors can result from the uniform stress drop condition. Third, based on previous studies of global earthquakes, we have a priori information on typical average stress drops in earthquakes [*Allmann and Shearer*, 2009; *Hanks*, 1977; *Shaw*, 2009]. Posing the inversion in terms of stress drop allows one to utilize this mechanical constraint directly in the inversion.

2. Mechanical Inversion of the Fault Slip Distribution From Geodetic Measurements

2.1. Introduction of the Uniform Stress Drop

[8] The uniform static stress drop of a circular fault can be calculated using the formula for a crack in an elastic medium [*Keilis-Borok*, 1957], $\Delta\sigma = \mu \frac{7\pi}{16} \frac{\overline{u}}{r}$, where μ, $\overline{u}$, and r are the elastic stiffness, average slip, and radius of the rupture area on the fault plane, respectively. Similar results for rectangular and elliptical cracks were obtained by *Knopoff* [1958] and *Eshelby* [1957]. These results assume a uniform stress drop.

[9] The analytical solutions cited above are for simple slip patch geometries. Our approach is to assume a uniform stress

Figure 1. Fault displacement and surface deformation assuming uniform static shear stress drop. The fault is the same in both cases with near north-south strike, 45° west dipping, 20 km width, and 20 km length. The radar interferograms are simulated similar to the Envisat ASAR data of European Space Agency in descending track with 23° incidence angle. The strike-slip and dip-slip components of the static stress drop are 3.0 and −5.0 MPa, respectively. (a) Displacement on a fault plane with the fault top at 3 km depth underground. (b) Displacement on a fault plane with the fault reaching the surface and other parameters unchanged. (c and d) The simulated line of sight ASAR radar interferograms in Figures 1a and 1b. (e) Displacement on a fault plane with the fault top at 3 km depth underground and four large patches locked. (f) Displacement on a fault plane with the fault top at 3 km depth underground and four large patches locked which is different with Figure 1e. (g and h) The simulated LOS ASAR radar interferograms in Figures 1e and 1f. The white rectangle denotes the surface projection of the fault plane and the black line shows the surface projection of the fault top. Note the different color cycle used in the interferograms. The distance is in units of km. The slip and deformation are in units of m.
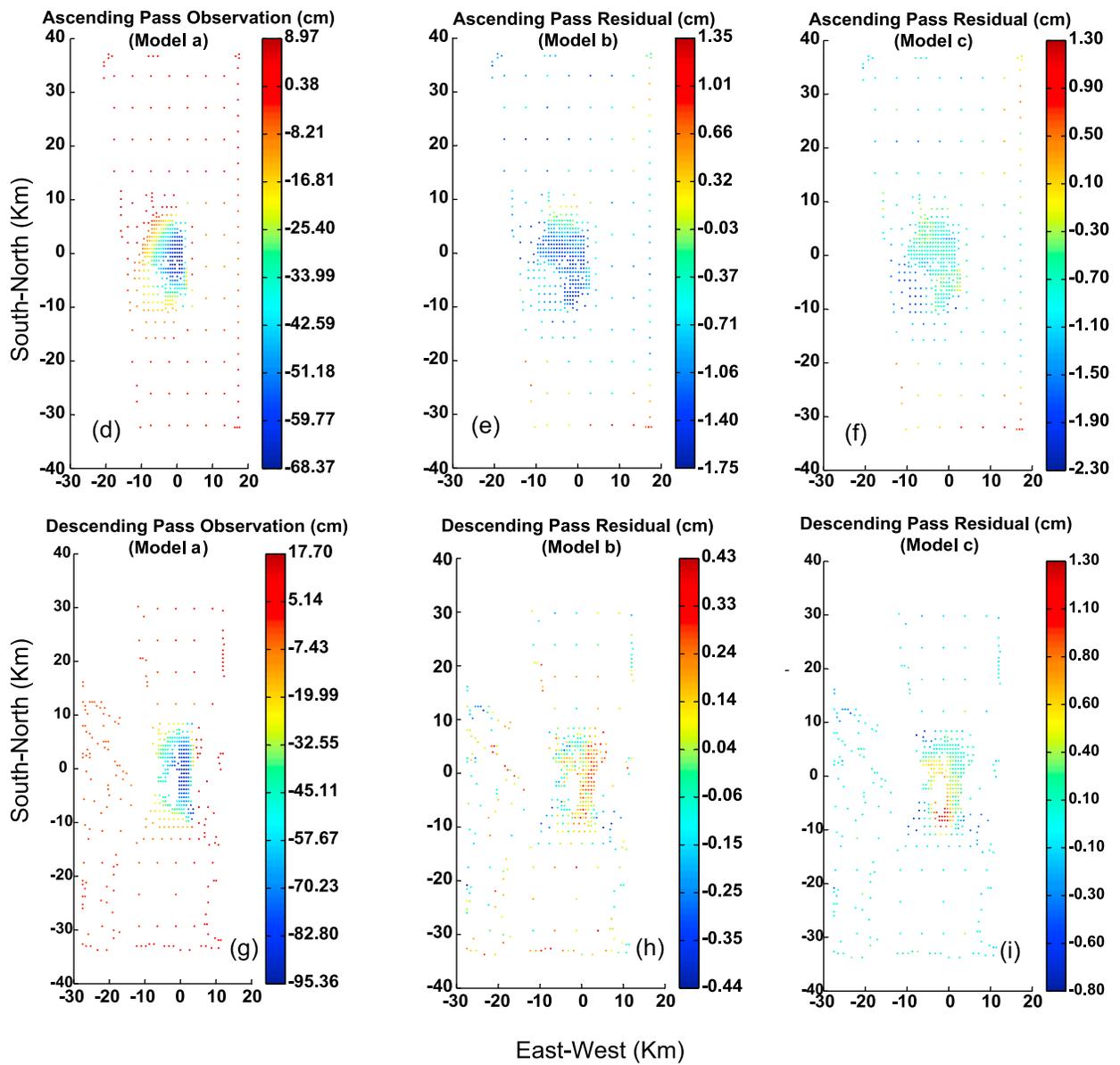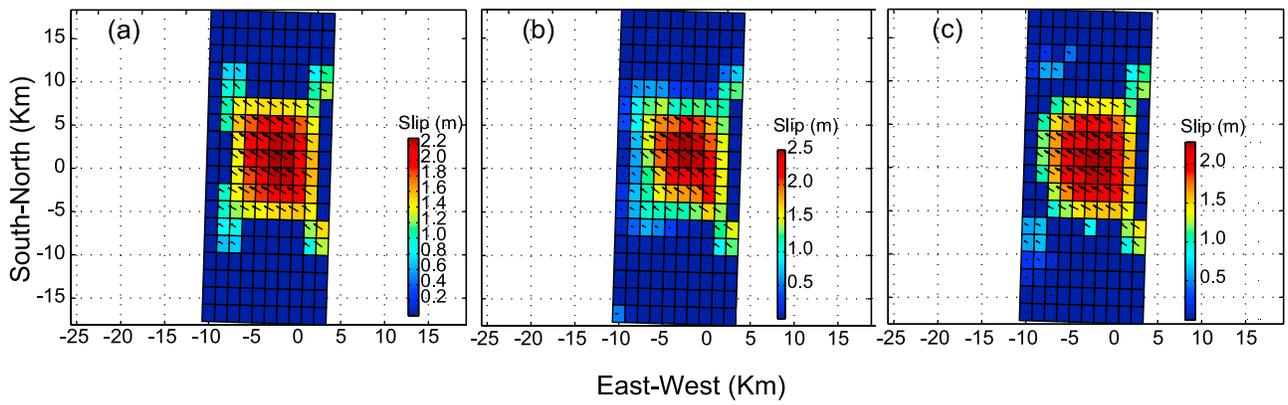
Figure 2

drop over a slip zone of arbitrary geometry and compute the resulting slip distribution using a boundary element technique. We discretize a slip zone of arbitrary shape on a planar fault into N rectangular slip patches. Using the *Okada* [1992] solution for a rectangular dislocation, we relate a 2Nx1 vector, $\Delta\tau$, of strike and dip components of the shear stress change on each patch to a 2Nx1 vector, s, of strike and dip components of slip on each patch through a kernel matrix, G_τ,

$$\Delta\tau = G_\tau s. \tag{1}$$

In a standard boundary element scheme, the slip on patches can be computed assuming a specified shear stress drop

$$s = G_\tau^{-1}\Delta\tau. \tag{2}$$

The *Okada* [1992] solution can also be used to relate slip on each patch to a Mx1 vector, d, of surface displacements through a kernel matrix, G_d,

$$d = G_d s. \tag{3}$$

Combining equations (2) and (3), the surface displacements are related to the specified shear stress drop as

$$d = G_d G_\tau^{-1}\Delta\tau. \tag{4}$$

The objective of the inversion is to estimate $\Delta\tau$. Before describing the inversion algorithm, we first illustrate the slip distributions resulting from a uniform stress drop model.

2.2. Simple Forward Models for the Uniform Stress Drop Assumptions

[10] In order to illustrate the effect of the uniform stress drop assumption on the fault slip distribution and ground deformation, we simulate four simple cases. We use a simple fault geometry with a single rectangular fault plane that strikes north-south, dips west 45°, and is 20 km wide by 20 km long. We examine (1) a blind normal fault with the top edge of the fault plane at a depth of 3 km (Figure 1a), (2) a normal fault that breaks the ground surface (Figure 1b), (3) a blind normal fault as in case 1 but with four large locked patches (Figure 1e), and (4) a blind normal fault as in case 1 and 3 but with four different locked patches (Figure 1f). The fault plane is discretized into 400 1 km by 1 km patches. In all of the cases the uniform stress drop is the same with a 3.0 MPa strike-slip component and a −5.0 MPa dip-slip component so that the forward modeling simulates a normal faulting with a minor right lateral component (negative stress drop indicates normal or left lateral faulting). We

generate simulated line of sight (LOS) radar interferograms from the computed slip distribution and the corresponding 3-D ground deformation of the four cases (Figure S1).[1]

[11] In the blind fault geometry case (Figure 1a), the slip area appears as a circular shape with peak slip of 2.69 m at the center. The seismic moment is ~2.17e+019 Nm and is equivalent to a M_w 6.89 event. In the second case the fault breaks the ground surface (Figure 1b), and the slip pattern is very different from that in the first case. The slip appears as an asymmetric half-disc shape with maximum slip at the surface that exceeds 4.11 m. The seismic moment in this case is ~3.05e+19 Nm and is equivalent to a M_w 6.99 event. We can see that the slip distribution and the seismic moment are quite different in the two cases, even with the same stress drop and the same fault geometry. The predicted surface deformation in the same SAR viewing angle (Envisat ASAR data of European Space Agency in descending track with 23° incidence angle) is different in both cases as well. The surface rupture case produces significantly larger deformation (Figure 1d) than the buried fault case (Figure 1c).

[12] Figures 1e and 1f illustrate the effects of irregular shape of the slipping patches. A large slip area in Figure 1e is concentrated in the middle part of the fault and smaller slip areas occur around the four locked patches. The model in Figure 1f shows two shallow high-slip areas separated by the shallow locked patch. In contrast to the model in Figure 1e, the middle part of the fault plane shows very small slip. The slip distribution is inherently smooth in all cases; however the magnitude of slip is largely controlled by the size of the patches that are allowed to slip. Figures 1g and 1h show the surface deformation in the view of radar satellites as Figures 1c and 1d. The models in Figures 1e and 1f illustrate the importance of identifying the location and size of locked and slipping areas on the fault in the inversion process.

2.3. Locked and Slipping Patches

[13] The above illustrations highlight two factors regarding the slipping area of the fault that need to be considered in an inversion in a real event. One is the extent of the fault surface participating in the rupture during an earthquake. Assuming a rectangular fault plane as in the above illustrations, we do not necessarily have a priori knowledge on which part of the fault plane slips in an earthquake. Different locking status of the fault plane patches will lead to different slip distributions. The second factor to be considered is the existence and extent of a surface rupture, given that the slip distributions are substantially different in the two scenarios of Figures 1a and 1b. The extent of surface rupture cannot always be determined from field observation for earthquakes in many cases. These issues raise the need for a decision

---

[1]Auxiliary materials are available in the HTML. doi:10.1029/2010JB007849.

Figure 2. The checkerboard model and the inversion result comparisons by two different inversion methods. (a) The checkerboard model by the Okada elastic solution with the uniform stress drop assumption. (b) The inversion result by the FBI method of *Fukuda and Johnson* [2008]. (c) The inversion result by the mechanical method with the uniform stress drop assumption. (d-f) The simulated ascending track data, the inversion residual by the kinematic FBI method in Figure 2b, and the mechanical method in Figure 2c. (g-i) The simulated descending track data, the inversion residual by the kinematic FBI method in Figure 2b, and the mechanical method in Figure 2c. Note that the simulated SAR data in LOS direction is perturbed by the realistic noise of the SAR data of this study.

process in the inversion scheme to identify patches as either locked or slipping.

2.4. From the Kinematic Solution to the Mechanical Solution Using the FBI Engine

[14] In the traditional kinematic slip inversion, damped least squares method is used to solve for the slip distribution with suitable smoothing to suppress unphysical slip oscillations. Moreover, the fast nonnegative least squares (FNNLS) method [*Bro and Jong*, 1997] or similar bounded value algorithms are commonly used to constrain the rake of the solution to fall within a range that is consistent with the tectonic stress field. The traditional approach is to find a slip distribution by minimizing an objective function like [see, e.g., *Fukuda and Johnson*, 2008]

$$\Phi(s) = \|\sum\nolimits_{\mathrm{d}}^{-\frac{1}{2}}(\mathrm{d} - \mathrm{G_d s})\|^2 + \beta^2 \|\mathrm{Ls}\|^2 . \qquad (5)$$

Here Σ_{d} is the data covariance matrix, d is the observation, G_{d} is the displacement Green's function, s is the fault slip, L is the smoothing operator (often taken to be the finite difference form of the Laplacian operator) and β is the smoothing factor.

[15] One could think of formulating the inversion in terms of shear stress change using equation (4) and minimizing the objective function

$$\Phi(\Delta\tau) = \|\sum\nolimits_{\mathrm{d}}^{-\frac{1}{2}}(\mathrm{d} - \mathrm{G_d G_\tau^{-1}}\Delta\tau)\|^2 . \qquad (6)$$

For a uniform stress drop (same stress drop on all slipping patches), the resulting slip distribution is inherently smooth, so it is not necessary to introduce a smoothing norm.

[16] We do not use an optimization approach to this inverse problem and therefore we do not explicitly seek to minimize the objective function (6). Instead, we develop a method based on the fully Bayesian inversion (FBI) engine [*Fukuda and Johnson*, 2008] developed for the purpose of the kinematic slip inversion. The FBI method introduces a fully probabilistic inversion method to simultaneously estimate the fault geometry, the slip distribution and the smoothing parameter objectively in a Bayesian framework. Through the sampling of a joint posterior probability density function of the smoothed slip and the likelihood function with a Markov Chain Monte Carlo (MCMC) method, the posterior probability distribution of the fault geometry parameters, smoothing parameters, data weights and slip distribution can be obtained simultaneously in the kinematic inversion. The details about the method are given by *Fukuda and Johnson* [2008]. Similarly, using the FBI method as an engine, the fault geometry, the stress drop and the slip distribution can be estimated simultaneously in the mechanical inversion. The major changes in this method relative to the FBI method for the kinematic inversion are the removal of the smoothing constraint and the adding of the inversion for uniform stress drop of the fault plane. The unknown parameters in the inversion are the strike and dip components of the uniform stress drop, strike, dip, and position of the fault plane. We also introduce a binary parameter for each slip patch that specifies whether the patch slips or not, which is similar to the method of *Yun et al.* [2006] for volcano deformation.

2.5. Realization of the Mechanical Inversion

[17] In the FBI-based uniform stress drop inversion, we seek an estimate of the posterior probability distribution of all unknown model parameters, given the data and their uncertainties. Let δ be the fault dip, θ the fault strike, (C_x, C_y, C_z) the coordinate of the center of the top edge of the rectangular fault, and b a Nx1 vector of binary locking parameters for each of the slip patches. To simplify the notation we put all of the geometry parameters into a vector, $g = [\delta, \theta, C_x, C_y, C_z]$. Let Σ_d be the covariance matrix of observation errors and σ^2 an unknown scale factor of Σ_d. Let G'_τ be the kernel matrix obtained by removing the columns and rows corresponding to locked patches from the kernel matrix G_τ defined in equation (1). Also, Let G'_d be the kernel matrix obtained by removing the columns corresponding to locked patches from the kernel matrix G_d, defined in equation (3). Then, the target posterior probability distribution is:

$$p(\Delta\tau, \sigma^2, g, b|d)$$
$$= \begin{cases} \frac{1}{Z}(\sigma^2)^{-N/2}\exp\left[-\frac{1}{2}f(\Delta\tau, g, \sigma^2, b)\right], \; for \; \sigma^2 > 0 \\ f(\Delta\tau, g, \sigma^2, b) = \frac{1}{\sigma^2}(d - G_d'G_\tau'^{-1}\Delta\tau)^T\sum\nolimits_{\mathrm{d}}^{-1}(d - G_d'G_\tau'^{-1}\Delta\tau), \\ \qquad 0, \; otherwise \end{cases}$$
$$\qquad (7)$$

where Z is a normalizing constant that is independent of other parameters. As with *Fukuda and Johnson* [2008], the formulation in (7) can be generalized to include multiple data sets, but we do not generalize it to include multiple fault segments for a single constant stress drop because the uniform stress drop assumption would not be valid in that case. However, it would be a simple extension of the current method to allow for different uniform stress drops on multiple fault segments in the inversion.

[18] As with *Fukuda and Johnson* [2008], we adopt the Metropolis algorithm to sample the posterior probability distribution. In this method, the model parameters are varied thousands of times and a collection of parameter values are selected according to the Metropolis rule. The collection of samples is used to represent the posterior probability distribution. The algorithm proceeds as follows:

[19] 1. Initialize the sample counter $t = 0$ and select an initial set of model parameters $\mathrm{x}^{(0)}$.

[20] 2. Set the parameter counter, $j = 1$.

[21] 3. Generate a candidate state by varying the jth parameter. If the jth parameter is not a binary parameter from b, select candidate x_j' from a 1-D uniform distribution over the interval $[\mathrm{x}_j^{(t)} - \delta\mathrm{x}_j, \mathrm{x}_j^{(t)} + \delta\mathrm{x}_j]$ where $\delta\mathrm{x}_j$ scales the step size of the Markov Chain along the jth coordinate direction in the parameter space. If the jth parameter is a binary parameter from b, switch the binary parameter.

[22] 4. If $\sigma^2 \leq 0$ reject the candidate state and remain at the current state: $\mathrm{x}^{(t+1)} = \mathrm{x}^{(t)}$. Then increase the parameter counter from j to $j + 1$ and return to step 3.

[23] 5. Compute the acceptance probability $P\mathrm{accept} = \min\left(1, \frac{p(x'|d)}{p(x^t|d)}\right)$.
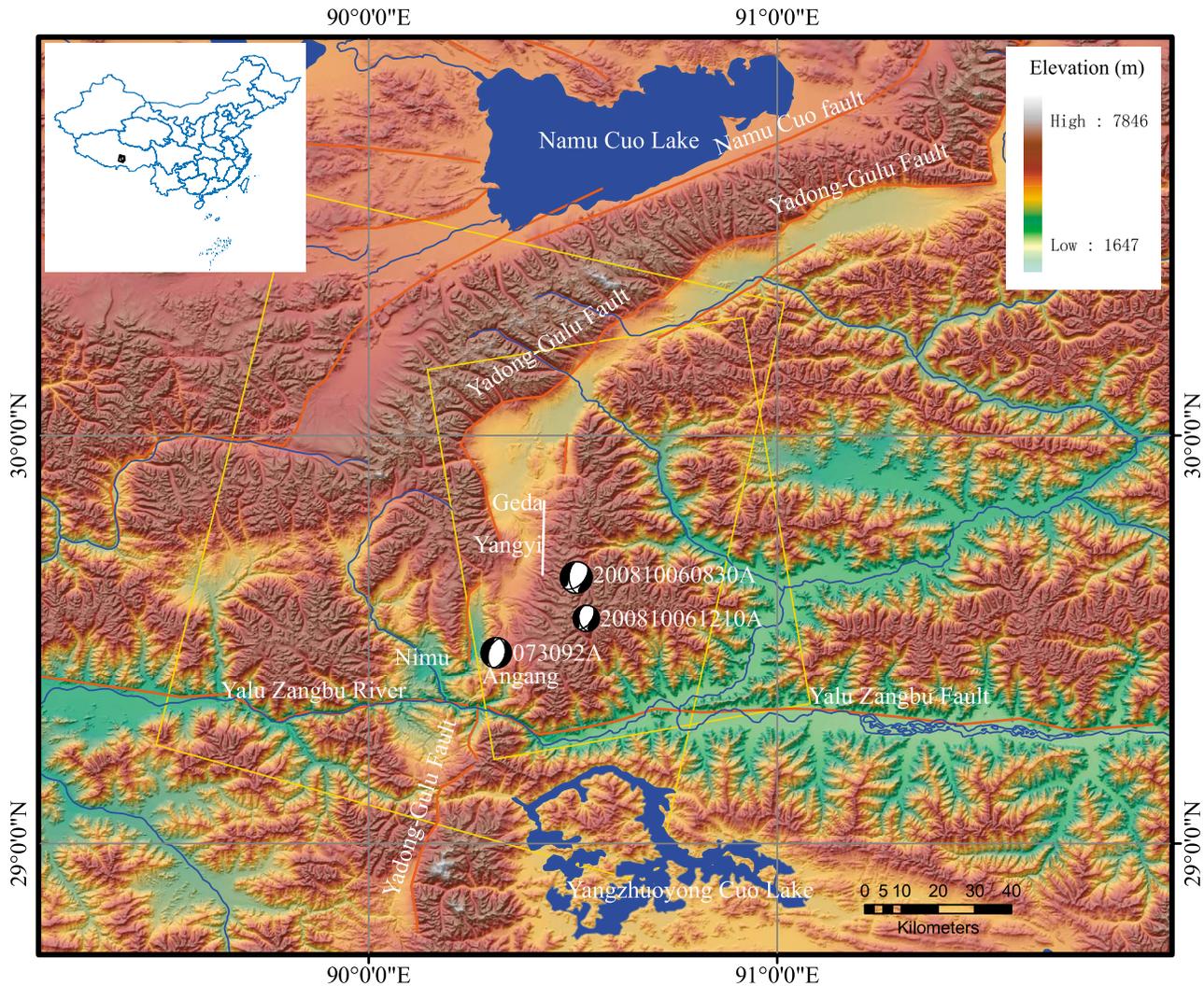
Figure 3. The tectonic background of the Dangxiong-Yangyi earthquake area. The red lines are the active faults in this area mapped by *Deng et al.* [2003] and revised in this study. The blue lines are the river system and the blue polygons are lakes close to this area. The yellow rectangles are the ground coverage of the two track SAR data. The white line is the fault location on the ground inferred from SAR data and the field investigation. The background is the SRTM DEM data. The inset map shows the location of the earthquake on a map of China. The three beach balls show the locations of three earthquakes in this area. The event "073092A" is the 1992 M_w 5.7 Nimu earthquake. The event "200810060830A" and event "200810061210A" are the main shock of the Dangxiong-Yangyi M_w 6.3 earthquake and its M_w 5.2 aftershock. The focal mechanism of the earthquakes is from the Harvard solution at http://www.globalcmt.org.

[24] 6. Generate a random number u from a uniform distribution over the interval [0, 1], $U(0, 1)$: $u \sim U(0, 1)$.

[25] 7. If $u \leq P\text{accept}$, then accept the candidate state x': $x^{(t+1)} = x'$. If $u > P\text{accept}$, then reject the candidate state and remain at the current state: $x^{(t+1)} = x^{(t)}$.

[26] 8. Increase the parameter counter from j to $j + 1$. If j is less than the number of parameters, return to step 3. Otherwise, increase the sample counter from t to $t + 1$ and return to step 2.

[27] Note that the displacement and stress Green's functions (G_d, G_τ) need to be computed only when the fault geometry parameters are changed. This is the most time-consuming step in the computation.

[28] After about 10^6 iterations, we can obtain a set of acceptable solutions. The Markov Chain convergences on the solution after a series of burn-in samples, which are dependent on the initial model guess, are computed. After discarding these burn-in samples, the mean and standard deviation of model parameters can be computed as by *Fukuda and Johnson* [2008]. Note that the efficiency of the algorithm depends partly on how close the initial model state is to the mean of the posterior distribution. We have

Figure 4. Field photos of the Dangxiong-Yangyi earthquake. (a) Surface fissure at the southern site (see Figure 3 for approximate location). The view is toward the south. (b) Close-up of Figure 4a with tape measure for scale showing an extensional fissure of ~15 cm. (c) Surface rupture at the northern site viewed toward the north and (d) close-up of Figure 4c indicating a vertical slip ~20 cm. The surface features show almost pure normal faulting. Note that the locations of the sites are only for reference and there are no exact coordinates available because of an instrument failure when we implemented the field investigation.

found that a good way to achieve a fast convergence of the inversion is to run a kinematic slip inversion first and use the optimal solution from this as the initial state for the mechanical inversion.

2.6. Checkerboard Resolution Test of the Mechanical Inversion

[29] In order to illustrate the method and assess the ability to resolve fault slip, we design a checkerboard model and invert for the parameters using the proposed method (Figure 2). The checkerboard is designed by assuming uniform stress drop and locking some patches so that the slip distribution is obviously heterogeneous compared with the simple models in Figure 1, but with only one dominating asperity. The fault plane strikes north-south and dips 45° to the west. Synthetic surface displacements are generated using equation (4) with imposed uniform dip and strike components of shear stress drop of −5.5 and 2.5 MPa,

Figure 5. InSAR observation of the Dangxiong-Yangyi earthquake. (a) The ascending track interferogram. (b) The descending track interferogram. The positive deformation corresponds to movement away from the satellite in both Figures 5a and 5b. (c and d) The covariance model of the resampled points from the ascending track interferogram and the descending track interferogram. Note that the covariance of the ascending track data is dramatically larger than the covariance of the descending track data. This indicates that the ascending track data has heavier atmospheric noise. (e and f) The semivariograms of the ascending track interferogram and the descending track interferogram. The blue lines are the experimental semivariogram in 10 directions. The green lines and the red lines are the modeled semivariogram in 10 directions using the exponential model and J-Bessel model, respectively. The ascending track data covariance model is derived from the J-Bessel model (red) and the descending track data covariance model is derived from the exponential model (green).

respectively (positive indicates reverse and right lateral sense of shear). Noise is added to the simulated InSAR data with the spatially correlated noise using the full covariance matrix of the real InSAR data of this study [*Sun et al.*, 2008]. We also invert for the fault slip using the kinematic fully Bayesian inversion method [*Fukuda and Johnson*, 2008] and the standard least squares method for comparison. The geometric parameters are fixed except for the fault dip. Both inverse methods recover the true dip angle of 45°. The new uniform stress inversion method predicts a slip distribution
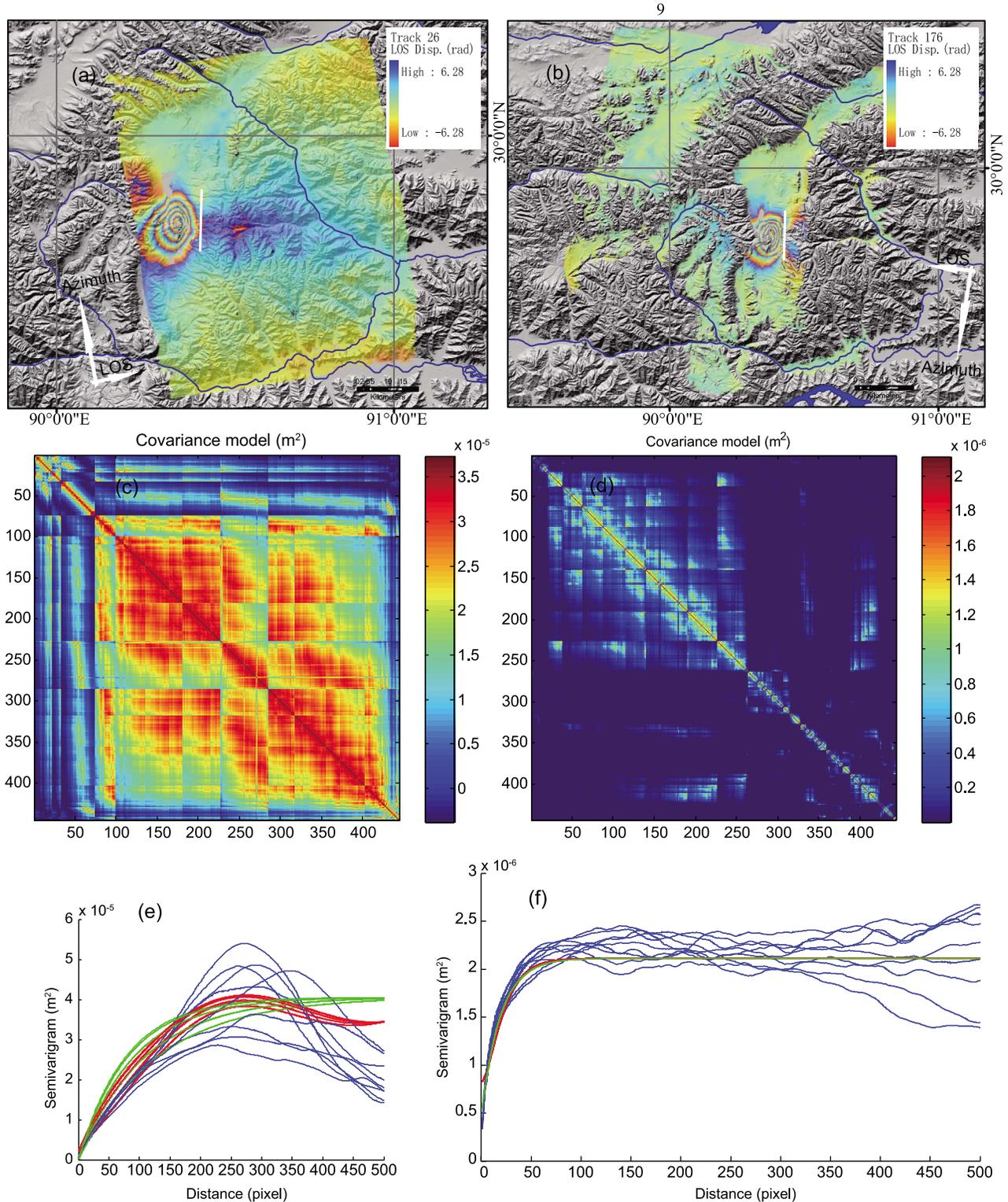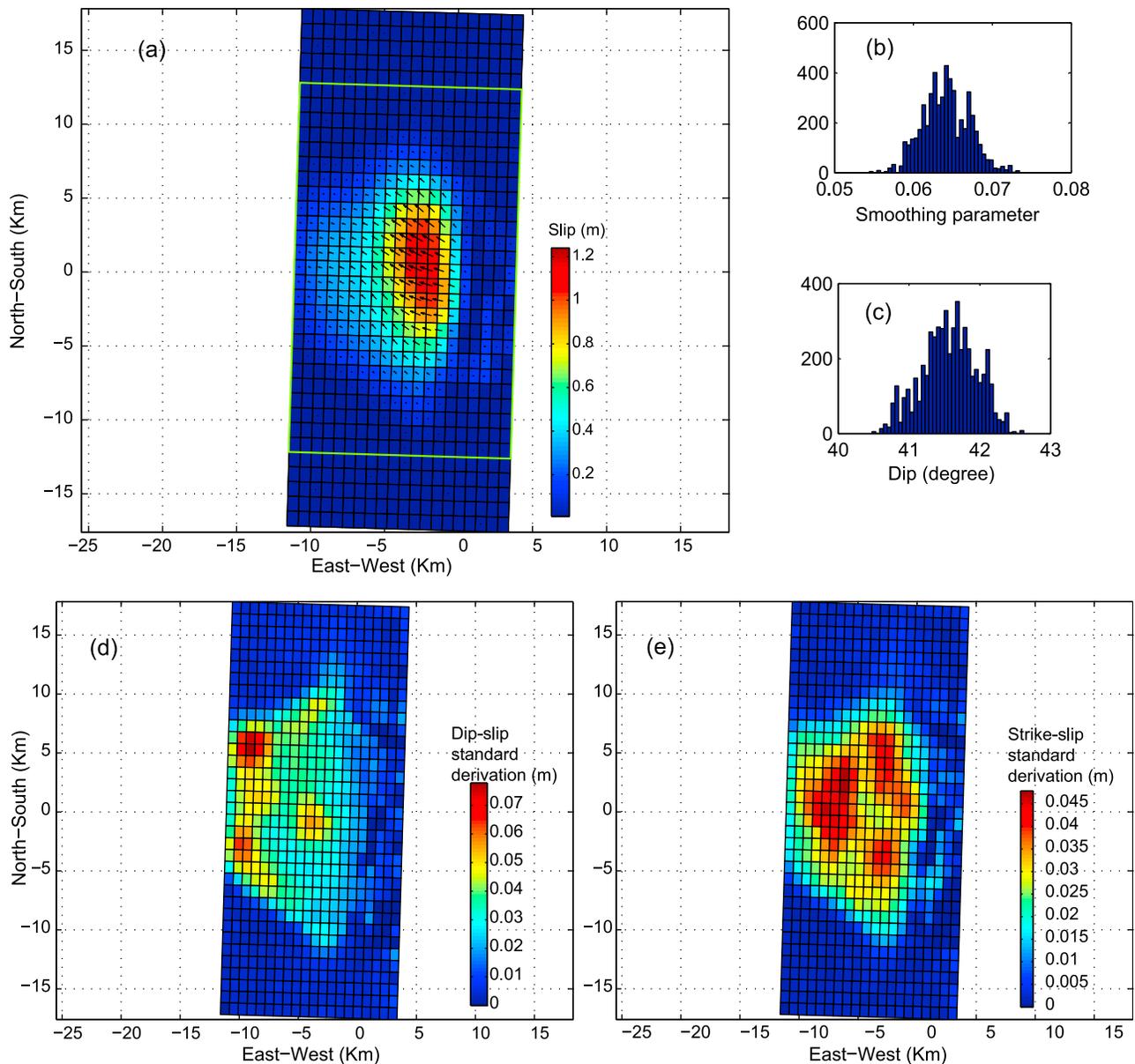

Figure 5

Figure 6. Slip distribution model of the Dangxiong-Yangyi earthquake from the FBI kinematical inversion with the tight rake constraint. (a) The slip distribution model. The green box shows the fault area used in Figures 10a and 12a. The color scale is set for slip magnitude range of 0–1.25 m. (b) The smoothing parameter distribution histogram. (c) The dipping angle distribution histogram. (d and e) The standard derivations of the dip-slip component and the strike-slip component.

that is very similar to the true slip distribution (Figure 2c). The inversion recovers the true values for stress change with estimates of −5.46 ± 0.01 MPa and 2.33 ± 0.01 MPa. The small uncertainties are because we assume uniform stress drop in the ideal model and the InSAR data simulation (no stress heterogeneity allowed). The kinematic FBI inversion produces a larger slip gradient than that of the mechanical inversion and slightly over predicts the peak slip value (Figure 2b). The kinematic inversion slip distribution is somewhat over smoothed because of the Laplacian smoothing prior. The standard constrained least squares inversion shows very similar results to the kinematic FBI inversion (Figure S2). All of the methods recover the true slip in the top few rows of patches, however, neither model is able to resolve the fault slip well in the bottom rows of slip patches.

3. The Dangxiong-Yangyi (Tibet) Earthquake and Inversion of InSAR Data

3.1. Tectonic Setting of the Dangxiong-Yangyi Earthquake

[30] The 6 October 2008 Dangxiong-Yangyi M_w 6.3 earthquake occurred on the central section of the Yadong-Gulu rift of southern Tibet, where normal faulting dominates the seismic behavior with faults dipping to the east and west
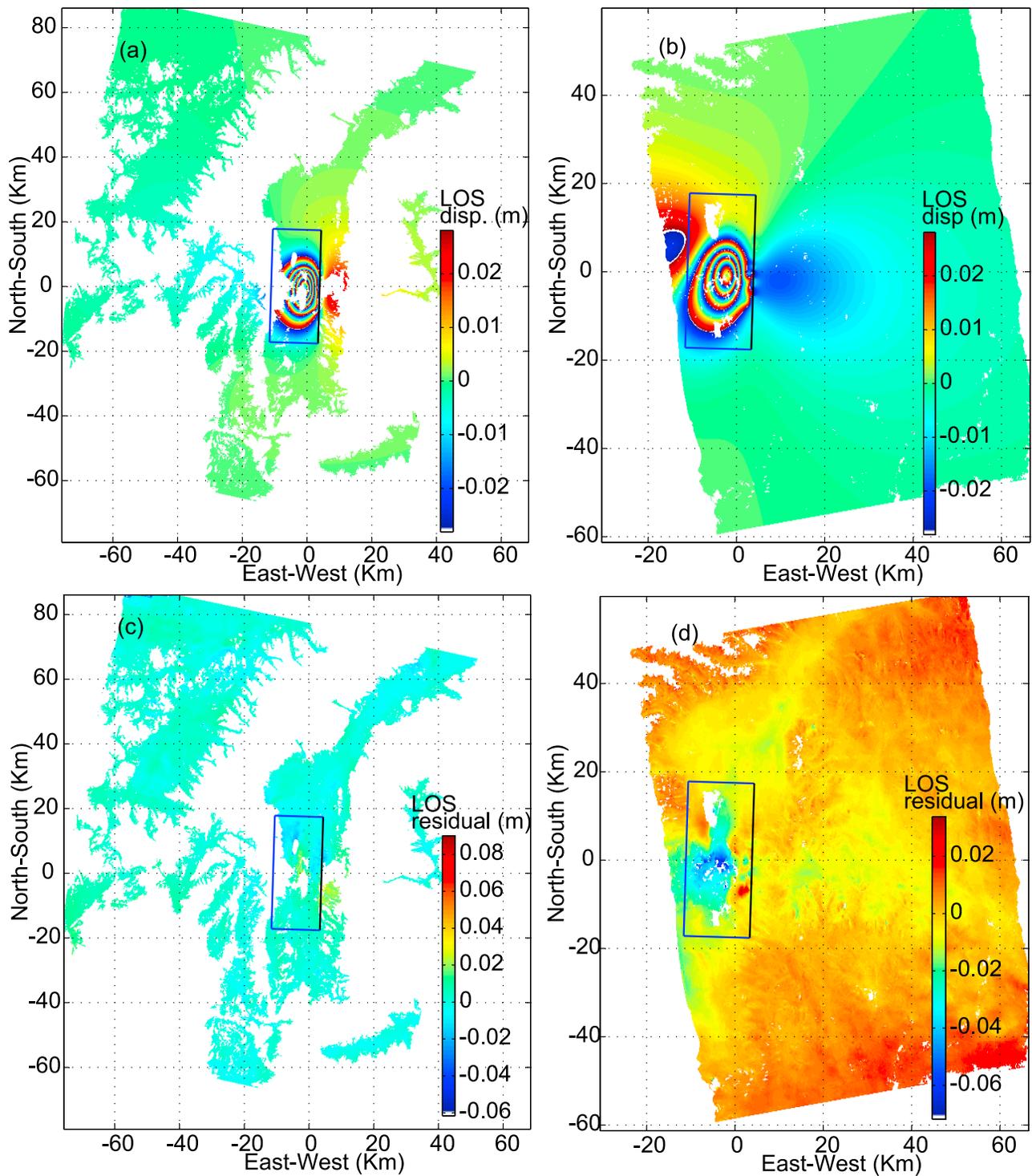
Figure 7. InSAR deformation field prediction using the slip distribution model of Figure 6a. (a and b) The predicted descending and ascending track interferograms wrapped into 0.56 cm cycles. (c and d) The LOS residuals after removing the predicted interferograms from the observations in Figures 5b and 5a. The blue box denotes the fault surface projection on the ground with the black line as its top.

[Armijo et al., 1986]. The system is inferred to be one of the seven major rift zones in southern Tibet, which accommodate east-west extension. The Yadong-Gulu graben is one of the most active rifts with an opening rate of 6.5 ± 1.5 mm yr^{-1} inferred from GPS data [Chen et al., 2004]. On

20 July 1992, a M_w 5.7 normal faulting earthquake occurred southwest of the Dangxiong-Yangyi earthquake on the west side of the rift (Figure 3).

[31] After the 2008 earthquake, we conducted a field investigation around the Yangyi basin and observed clear
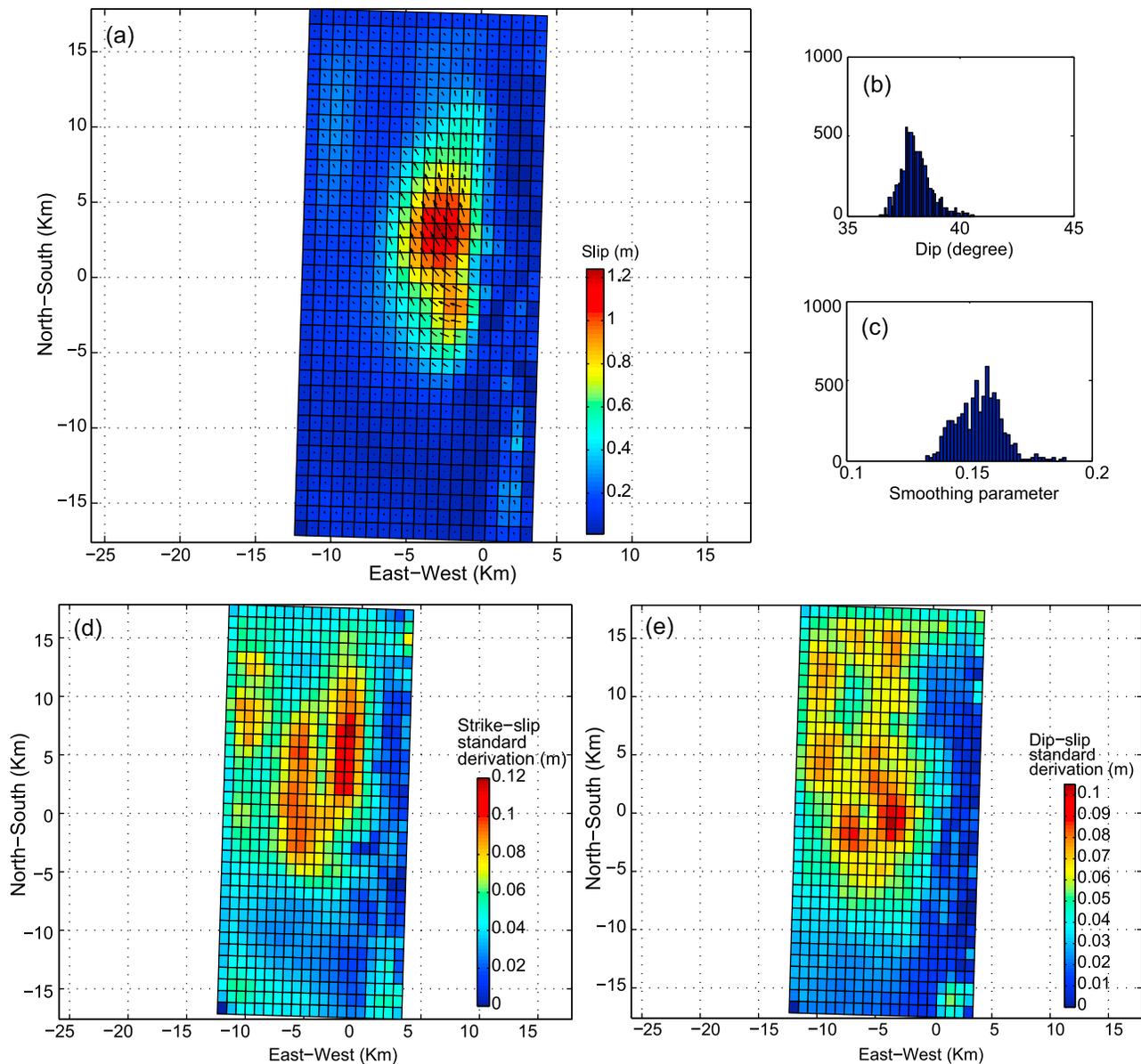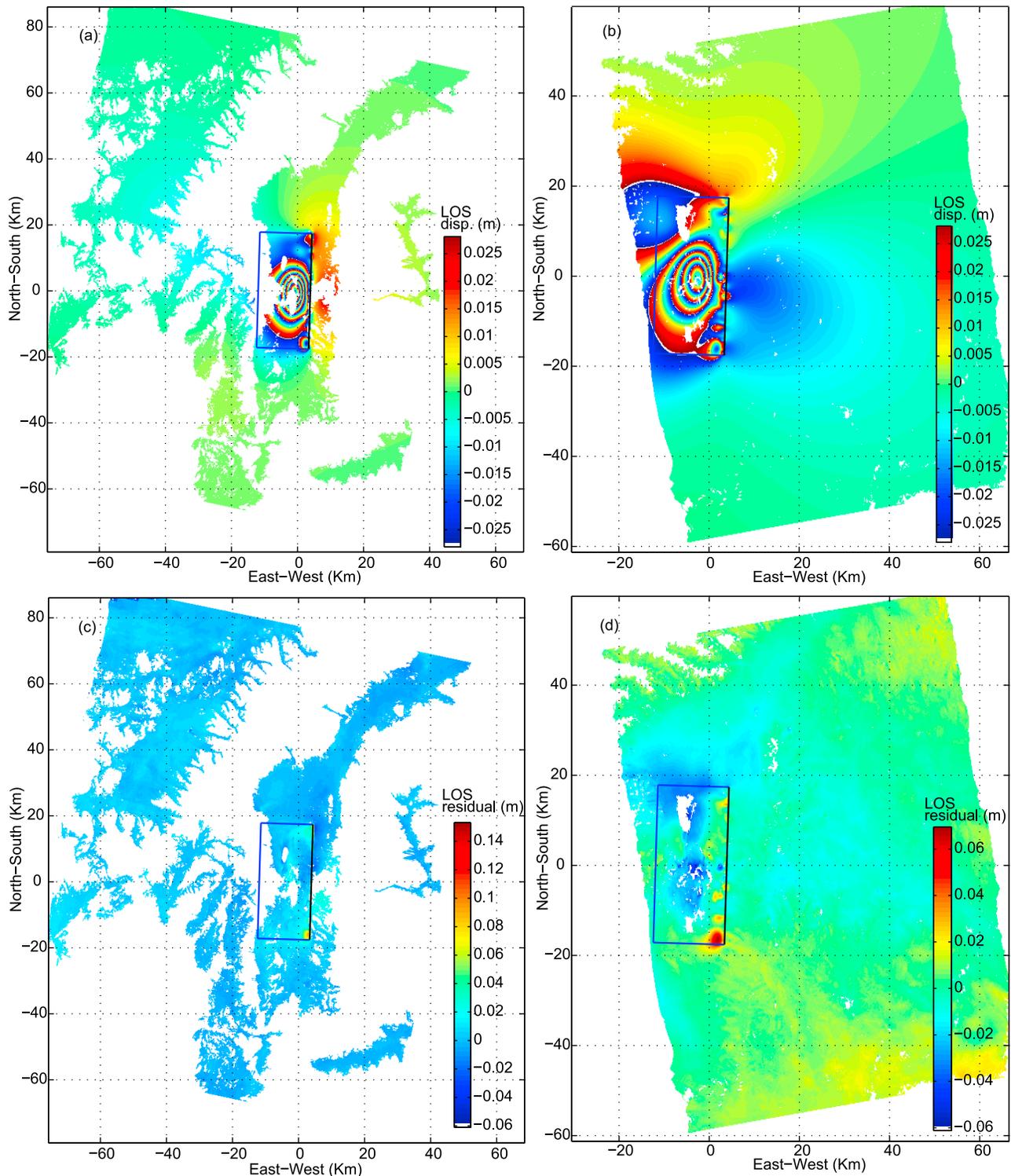
Figure 8. Slip distribution model of the Dangxiong-Yangyi earthquake from the FBI kinematical inversion without the tight rake constraint. (a) The slip distribution model. The color scale is set for slip magnitude range of 0–1.25 m. Note the strong rake variation on the fault plane. (b) The dipping angle distribution histogram. (c) The smoothing parameter distribution histogram. (d and e) The standard derivations of the strike-slip component and the dip-slip component.

surface deformation features, which show mainly west dipping normal fault surface ruptures at two sites along the basin edges (Figure 4). There is no significant strike-slip component of motion observable in the ground ruptures. The field work indicates that some slip propagated to the surface even though the surface features are only localized in two short segments (about 3 km long each). The evidence of surface rupture is important because SAR data alone is often not able to detect the surface rupture of moderate-size earthquakes, if the coherence of interferograms is very low near the fault. The field observations will be compared with InSAR data modeling.

3.2. SAR Data and Processing

[32] We acquired ASAR radar data from Envisat satellite of European Space Agency for interferometric mapping of the earthquake deformation. There are two pairs of SAR data acquisitions available for InSAR processing with small temporal and spatial baselines. One is the swath IS6 data acquired along track 26 on an ascending orbit track on 23 April 2008 and 15 October 2008, with a ~60 m perpendicular baseline. The other one is the IS2 data along track 176 on a descending track acquired on 21 September 2008 and 26 October 2008, with a ~220 m perpendicular baseline. We processed the data with the ROI_pac software package developed at JPL/Caltech [*Rosen et al.*, 2004] and

Figure 9. InSAR deformation field prediction using the slip distribution model of Figure 8a. (a and b) The predicted descending and ascending track interferograms wrapped into 0.56 cm cycles. (c and d) The LOS residuals after removing the predicted interferograms from the observations in Figures 5b and 5a. The blue box denotes the fault surface projection on the ground with the black line as its top.

the 3 arc sec SRTM DEM [*Farr et al.*, 2007] is used for topographic phase removal. The residual orbital phase and the contribution from the signals of systematic atmospheric stratification are estimated and removed with a least squares method assuming a close to zero phase change in the far field. Because the coseismic deformation area is small compared with the standard frame extent of Envisat ASAR data, the orbital phase residual is assumed to be a linear ramp across the
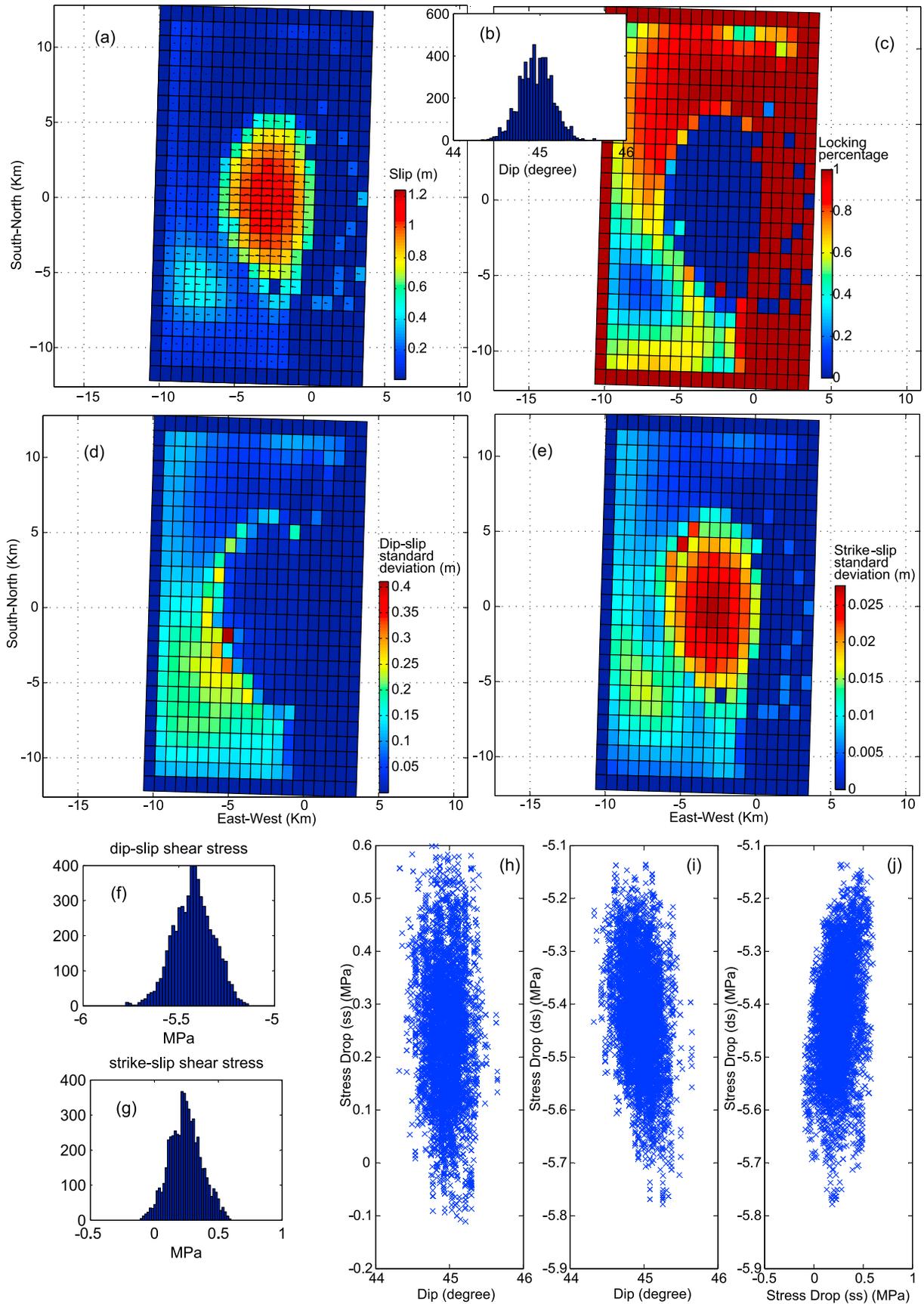
Figure 10

interferogram. The atmospheric stratification signals are estimated considering its correlation with the DEM data. We iteratively estimate and remove both of the nontectonic signals before data sampling and inversion. We also construct the full covariance matrix using a method described by *Sun et al.* [2008] to weigh the data subsampled with the quad-tree algorithm [*Jonsson et al.*, 2002]. The matrix considers not only the variance of the SAR data in its diagonal part, but also the spatial correlations of InSAR observations characterized by the nondiagonal terms (Figures 5c and 5d). In this study, we adopt a 2-D structure of the correlation noise, the so-called anisotropic distribution of atmospheric noise, which considers the noise variation with both distance and orientation (Figures 5e and 5f). In general, the fringe pattern is simple and we may infer that there is only one fault surface involved in the earthquake. The two interferograms show a clear concentric fringe pattern representing a zone of range increase to the west, in the hanging wall of the seismogenic fault where fringes are denser than on the east side. The descending and ascending track imaging geometry show very similar line of sight fringes indicating mainly vertical motion appearing in the earthquake faulting with hanging wall side subsidence and footwall side uplift. We note that the ascending track interferogram has a "stomach" shape compared to the more symmetric shape of the descending track range change pattern (Figure 5a).

### 3.3. Slip Inversion of the Dangxiong-Yangyi Earthquake

[33] Based on the InSAR observations and the inversion method described in section 2.4, we model the coseismic deformation field of the Dangxiong-Yangyi earthquake using both the mechanical inversion method developed in this study and, for comparison, a kinematic inversion using a method with objective smoothing (fully Bayesian inversion method) [*Fukuda and Johnson*, 2008]. We also use the traditional constrained least squares inversion for more comparisons. For the kinematic inversion, we adopt a rectangular fault plane with fixed dimensions of 35 km length along strike and 20 km width in the downdip direction. The location of the surface trace of the fault can be easily inferred from the interferograms and we fix its location and strike in the inversion. Because we observed some surface ruptures in the field, the top depth of the fault is set to be zero. Thus, the only unknown geometric parameter to estimate in the inversion is the fault dip. We discretize the rectangular fault into 700 1 km by 1 km patches. In the kinematic FBI method, we constrain the fault rake between −90° and −45° (right lateral rake is negative). This is equivalent to assuming the dip component of slip is larger than the strike component to be consistent with the focal mechanism of the earthquake and the tectonic environment of this area. Hereafter, we refer to this as the "tight rake constraint."

[34] The mechanical inversion requires more computation time than the kinematic FBI method for the same number of inversion steps. As in the kinematic FBI method, the mechanical inversion computes Green's function whenever the fault geometry is adjusted, but the mechanical inversion also has to compute the slip distribution by inverting the matrix in equation (2), $s = G_\tau^{-1}\Delta\tau$, for every stress drop sampling. To reduce the inversion time in the mechanical inversion, we adopt a smaller fault plane by using the slip area from the kinematic inversion as a guide such that the fault plane is large enough to include all of the patches with slip larger than ~3 cm. We assume the fault dimensions to be 25 km in length along strike and 20 km in width in the downdip direction. We again discretize the fault into 1 km by 1 km patches. In addition, we locked the bottom and edge patches. We start the inversion with a preliminary stress drop value of the strike and dip components based on the stress drop from the kinematic inversion results and use several different stress drop steps ranging from 1 to 0.01 MPa to restart the inversion to be assured that the final posterior distributions are independent of the initial starting values. After 5000 iterations with 5000 Green's function computations (again, only the dip angle is sampled) and 2.5×10^6 computations of $s = G_\tau^{-1}\Delta\tau$ (equation (2)), we find that the estimate of the posterior probability density function stabilizes and does not change significantly with more samples. We discard the first 50 samples, which reflect the initial "burn-in" process for reaching the stable posterior probability density values. The remaining samples are used to evaluate the probability distribution of the dip angle, stress drop components and the slip distribution.

3.4. Inversion Results of the Dangxiong-Yangyi Earthquake

[35] The kinematic inversion with the tight rake constraint (−90° to −45°) shows maximum slip of 1.10 m at 5~6 km depth (Figures 6 and 7). There is a small, right lateral strike-slip component, but the dip slip is significantly larger everywhere because of the tight rake constraint. The kinematic inversion without the tight rake constraint (−90° to 0°) shows larger strike-slip offsets than the dip-slip component at the bottom of the peak slip area (Figures 8 and 9). The tightly constrained kinematic inversion shows an elliptical asperity with ~15 km length and ~8 km width. There is some small slip close to the surface reaching ~20–25 cm which is consistent with our field investigation (Figure 4). The mean estimated dip angle is 41.6° and the seismic moment is 2.97e+18 Nm, corresponding to a M_w 6.3 earthquake (Figures 6 and 7). In contrast, the mean dip angle is 37.9° and the maximum slip and the seismic moment are 1.2 m and 4.64e+18 Nm (M_w 6.4), respectively, when the rake constraint is relaxed to −90° to 0° (Figures 8 and 9). The model without the tight rake constraint shows a better

Figure 10. Slip distribution model of the Dangxiong-Yangyi earthquake from the mechanical inversion. (a) The slip distribution model. The color scale is set for slip magnitude range of 0–1.25 m. The fault dimension is the same as the green box in Figure 6a. (b) The dipping angle distribution histogram. (c) The locking percentage of the fault patches by averaging the binary parameters of the accepted models excluding those burning in samples. If a patch is locked in all of the accepted models, its locking percentage is 1.0. On the contrary, the value would be 0.0 if it is unlocked. (d and e) The standard derivations of the dip-slip component and the strike-slip component. (f and g) The dip-slip shear stress distribution histogram and the strike-slip shear stress distribution histogram. (h-j) The scattering distributions of the dipping angle and the uniform stress drops in two dimensions. They show the trade-off among the three inverted parameters.
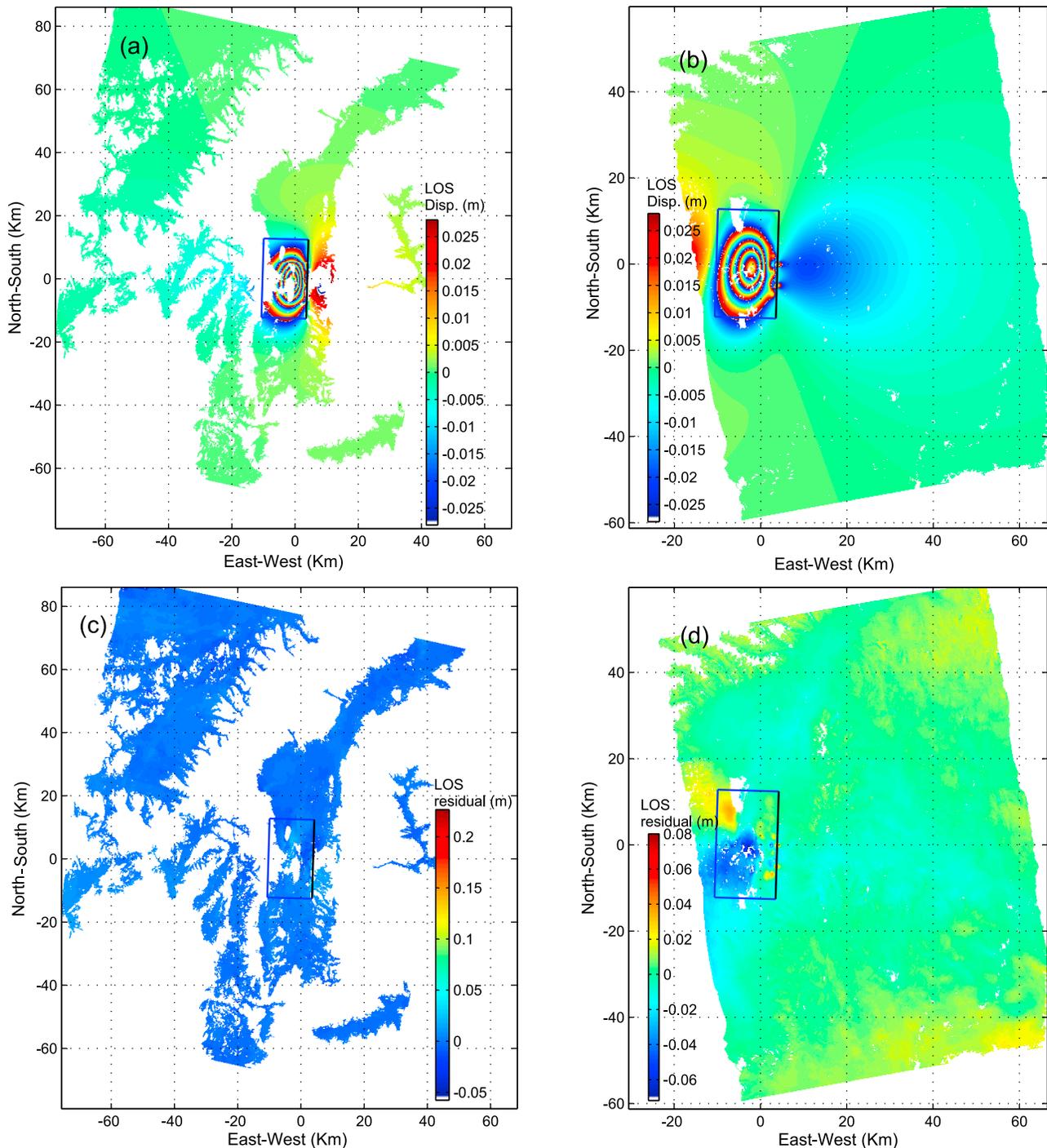
Figure 11. InSAR deformation field prediction using the slip distribution model of Figure 10a. (a and b) The predicted descending and ascending track interferograms wrapped into 0.56 cm cycles. (c and d) The LOS residuals after removing the predicted interferograms from the observations in Figures 5b and 5a. The blue box denotes the fault surface projection on the ground with the black line as its top.

fit with a maximum line of sight residual of 5.6 cm than the tight rake constraint model with a maximum line of sight residual of 6.5 cm in the ascending pass using the sampled data points. The residuals for the descending track data are nearly equal in both cases. The weighted residual sum of squares (WRSS) increased significantly from 1486 to 2901, correspondingly, for both data sets. We also use the same

fault model and the same smoothing parameter in Figure 8 to invert for the slip distribution using the traditional fast nonnegative least squares method [*Bro and Jong*, 1997]. It shows a similar slip distribution as in Figure 8, but with more variable rake angles (Figure S3).

[36] The mechanical inversion results (Figures 10 and 11) show a roughly elliptical asperity that is ~12 km in length

and ~9 km in width, which is somewhat smaller than the asperity from the kinematic inversions. There are two small patches with slip reaching ~40 cm near the ground surface. The location of shallow slip is consistent with our field investigation although the magnitude of modeled slip is larger than observed in the field. Unlike the kinematic inversion, the mechanical inversion finds another large slip area in the southwest corner of the fault plane (Figure 10a), with peak slip of 0.48 cm. The summed seismic moment of this slip area is ~3.09e+017 Nm, corresponding to a M_w 5.66 earthquake. This slip patch could reflect slip in the largest aftershock (8.25e+16 Nm, M_w 5.27) that occurred several hours after the main shock according to the GlobalCMT solution (http://www.globalcmt.org). In order to show the confidence level of the locking status of the fault patches, we compute the locking percentage of the fault patches by averaging the binary parameters of the accepted models excluding those burning in samples (Figure 10c). The blue areas indicate the patches unlocked and the red areas indicate the patches locked in most of the iterations. In order to evaluate the trade-off effects among the geometry parameters and the stress drop components, we plot the scattering points of those parameters in 2-D spaces (Figures 10h–10j). We can see there are no significant correlations among the three parameters in the accepted models after excluding the burn-in samples.

[37] The mean and standard deviation of the dip angle and the maximum slip from the mechanical inversion are 45 ± 0.19° and ~1.13 m, respectively and the seismic moment is 2.98e+18 Nm (M_w 6.3). There is a small strike-slip component, but the slip is predominantly dip-slip. The mean and standard deviation of the strike-slip and dip-slip components of stress drop are 0.24 ± 0.13 MPa and −5.42 ± 0.10 MPa, respectively. The total stress drop is ~5.43 MPa with rake of 92.5° indicating almost pure normal faulting.

4. Discussion

4.1. Comparison of Kinematic and Mechanical Inversion Methods

[38] There are some advantages to the mechanical inversion method we introduce over the classical kinematic inversion for slip distribution using geodetic data. First, we present a simple way to avoid introduction of a smoothing operator, smoothing parameter, and selection method of the smoothing parameter. The slip distribution resulting from uniform stress drop is inherently smooth.

[39] Second, the mechanical inversion simplifies the problem of identifying strong correlations between fault slip and geometry parameters. The correlation between slip and geometry parameters leads to strong trade-offs in the kinematic slip inversion, rendering the FBI kinematic inversion practically intractable for the joint slip geometry problem. In the kinematic FBI inversion, each slip patch is free to take on any slip value over the interval $(-\infty, \infty)$. In the mechanical inversion, the correlation between slip is parameterized in terms of two components of stress drop and patch-locking binary parameters. Therefore, the model space that must be searched using a Monte Carlo inversion is much smaller in the mechanical inversion. As a consequence, although the mechanical inversion requires more computation time than the kinematic FBI method for the

same number of inversion steps as we describe in section 3.3, the mechanical inversion converges in a small number of iterations than the kinematic FBI inversion and is more efficient for inversions with unknown fault geometry.

[40] Third, in the mechanical inversion we do not require additional constraints on the rake using computationally costly nonnegative or bounded least squares inversion algorithms as is typical in conventional kinematic slip inversions. An obvious disadvantage to the mechanical inversion is that the uniform stress drop assumption precludes the ability to resolve highly heterogeneous slip. In reality, the stress drop may be heterogeneously distributed on a rupture surface, especially for large earthquakes where fault geometry is composed of many segments and asperities and the prestress may also be complex. In this case, the uniform stress drop assumption is not valid. Of course, the same is true for applying smoothing to ruptures whose slip distribution is very rough. One could generalize our algorithm to allow for spatially variable stress drop or different stress drops on different fault segments, but this will introduce more unknowns in the inversion.

4.2. Systematic Residuals in Ascending Pass Data

[41] From the kinematic and mechanical inversion results, we find that there are systematic residuals in all of the inversions on the hanging wall side of the fault in the ascending track data (track 26) (Figures 7d, 9d, and 11d). The residuals have the same LOS direction as the data in the ascending track but not in the descending track. The maximum LOS residuals in the descending track data approach ~3 cm but the distribution of the residuals is not systematic in all of the inversions. The ascending track residuals have similar spatial distributions in both the kinematic inversion with tight rake constraint (Figure 7d) and the mechanical inversion (Figure 11d). The residual in the kinematic inversion without tight rake constraint also shows systematic features (Figure 9d), but the residual pattern extends farther to the north and over a larger area than the other two inversions (Figures 11d and 7d). The different spatial distribution of the residuals in Figure 9d can be attributed to the change in rake across the rupture area in the kinematic inversion.

[42] The systematic residual cannot be attributed to vertical motion because it appears mainly in the ascending track data. The possible explanation of the residual is that it is a result of motion parallel to the azimuth direction of the descending data. According to the LOS direction of the residual, we infer that the motion reflects a right lateral component of slip. Note that the strike of the fault is almost parallel with the azimuth direction of the descending track data. Based on this observation, we invert the mechanical model residual from the ascending track data for fault slip with the kinematic FBI method using the same fault plane of the mechanical inversion. The inversion shows slip reaching ~0.48 m at a depth of ~5 km, which is somewhat deeper than the maximum coseismic slip depth and farther to the north (Figure 12). It is unlikely that this residual slip reflects postseismic afterslip because the main shock is mainly a normal faulting earthquake and therefore afterslip is expected to have similar slip sense. The source of the systemic residual remains unclear.
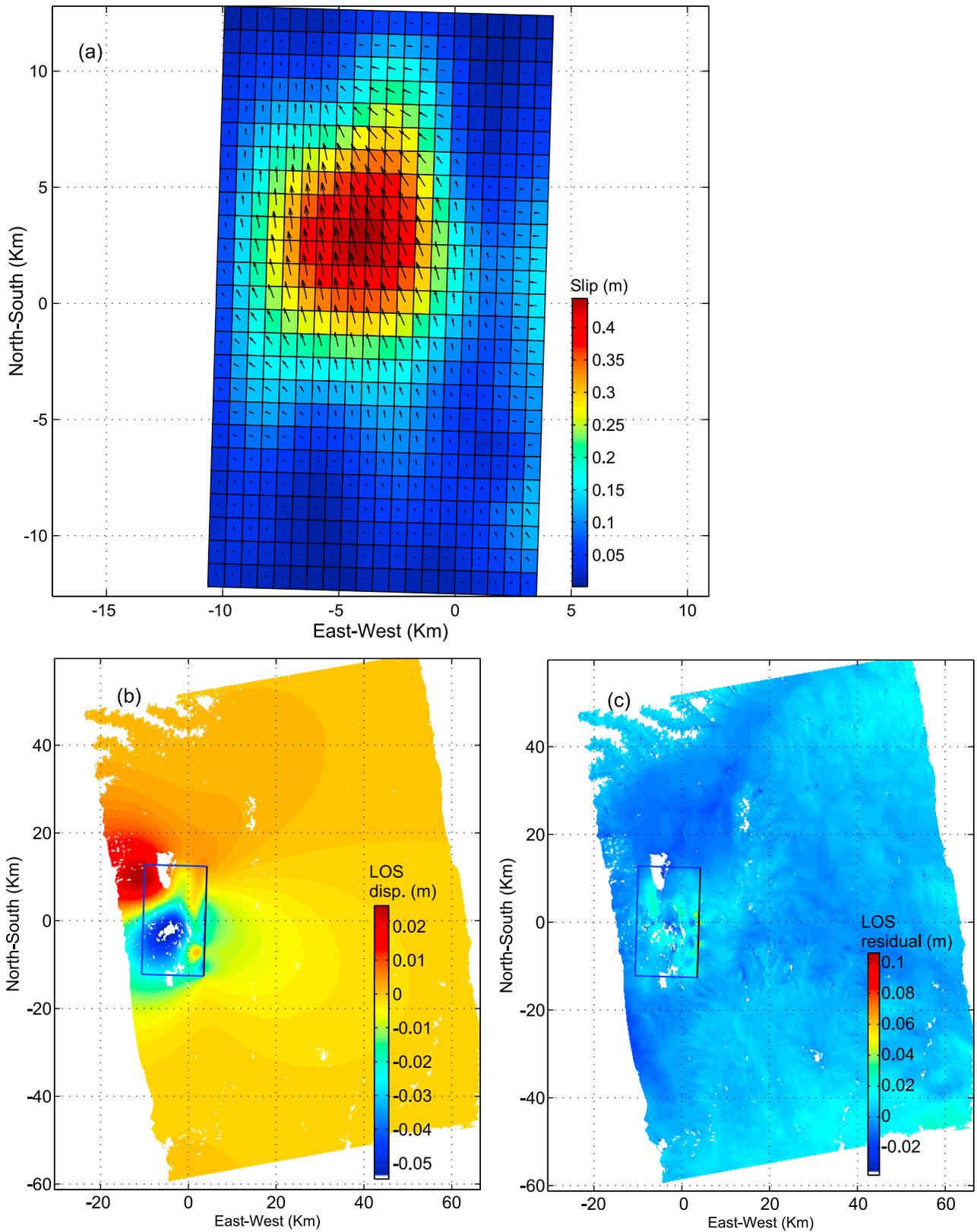
Figure 12. The slip distribution model by inverting the mechanical inversion residual in ascending pass. (a) The slip distribution model. The fault dimension is the same as the green box in Figure 6a. (b) The predicted ascending track LOS displacement. (c) The LOS residual after removing the predicted LOS displacement (Figure 12b) from the mechanical inversion residual in Figure 11d. The blue box denotes the fault surface projection on the ground with the black line as its top.

4.3. The Smaller Peak Slip Area on Fault Plane and Its Origin

[43] We found an isolated slip patch in the southwest corner of the fault plane (Figure 10a) in the mechanical inversion. This slip patch has peak slip of ~0.48 cm and is located ~5 km deeper than the main slip patch area. The summed seismic moment around this peak slip area is ~3.09e+017 Nm, corresponding to a M_w 5.66 earthquake. In the kinematic inversion, this slip patch is missing and the associated surface deformation is mapped instead into additional strike-slip offsets. This can be seen by comparing the results of the mechanical inversion with a kinematic inversion constrained to have only a dip component of slip. The result of this inversion is shown in Figure S4. We see that this inversion places some slip in the smaller slip area seen in the mechanical inversion. However, because of the effects of smoothing in the kinematic inversion, we do not see a distinct, separate slip area in the southwest corner of the fault. We argue that this smaller slip area could reflect slip from the largest aftershock recorded several hours after the main shock with moment 8.25e+16 Nm and magnitude M_w 5.27 (http://www.globalcmt.org).

5. Conclusions

[44] We develop a new method for the inversion of geodetic data utilizing the condition of uniform stress drop on the fault plane. Shear stress Green's functions are used to relate the stress drop and fault slip. We refer to the method as a mechanical inversion, to discriminate from the traditional kinematic inversion techniques that do not assume a relationship between stress and slip on the fault. An important property of the new method is that a smoothing norm of the slip vector need not be specified because the uniform stress drop condition results in inherently smooth slip distributions. In order to simultaneously solve for the fault geometry, the distribution of locked and slipping patches, fault slip and stress drop, we use a Bayesian framework borrowed from the full Bayesian inversion method of *Fukuda and Johnson* [2008].

[45] The Dangxiong-Yangyi earthquake is an important event in the Yadong-Gulu rift. The earthquake reflects the strong east-west extension of southern Tibet. By using the new mechanical inversion method developed in this study, we identify a $45 \pm 0.19°$ west dipping fault with a maximum net slip of ~1.13 m at a depth of ~5 km. The strike-slip and dip-slip stress drop are estimated to be 5.42 ± 0.10 MPa and 0.24 ± 0.13 MPa respectively, which fall within the typical range of earthquake stress drops of *Scholz* [2002] and *Allmann and Shearer* [2009].

References

Allmann, B. P., and P. M. Shearer (2009), Global variations of stress drop for moderate to large earthquakes, *J. Geophys. Res.*, *114*, B01310, doi:10.1029/2008JB005821.

Armijo, R., P. Tapponnier, J. L. Mercier, and T. L. Han (1986), Quaternary extension in southern Tibet: Field observations and tectonic implications, *J. Geophys. Res.*, *91*(B14), 13,803–13,872, doi:10.1029/JB091iB14p13803.

Árnadóttir, T., and P. Segall (1994), The 1989 Loma Prieta earthquake imaged from inversion of geodetic data, *J. Geophys. Res.*, *99*(B11), 21,835–21,855, doi:10.1029/94JB01256.

Bro, R., and S. D. Jong (1997), A fast non-negativity-constrained least squares algorithm, *J. Chemometr.*, *11*(5), 393–401, doi:10.1002/(SICI)1099-128X(199709/10)11:5<393::AID-CEM483>3.0.CO;2-L.

Chen, Q. Z., J. T. Freymueller, Z. Q. Yang, C. J. Xu, W. P. Jiang, Q. Wang, and J. N. Liu (2004), Spatially variable extension in southern Tibet based on GPS measurements, *J. Geophys. Res.*, *109*, B09401, doi:10.1029/2002JB002350.

Deng, Q., P. Zhang, Y. Ran, X. Yang, W. Min, and Q. Chu (2003), Basic characteristics of active tectonics of China, *Sci. China Ser. D*, *46*(4), 356–372.

Du, Y., A. Aydin, and P. Segall (1992), Comparison of various inversion techniques as applied to the determination of a geophysical deformation model for the 1983 Borah Peak earthquake, *Bull. Seismol. Soc. Am.*, *82*(4), 1840–1866.

Eshelby, J. D. (1957), The determination of the elastic field of an ellipsoidal inclusion, and related problems, *Proc. R. Soc. London A*, *241*(1226), 376–396, doi:10.1098/rspa.1957.0133.

Farr, T. G., et al. (2007), The Shuttle Radar Topography Mission, *Rev. Geophys.*, *45*, RG2004, doi:10.1029/2005RG000183.

Fialko, Y. (2004), Probing the mechanical properties of seismically active crust with space geodesy: Study of the coseismic deformation due to the 1992 M_w 7.3 Landers (southern California) earthquake, *J. Geophys. Res.*, *109*, B03307, doi:10.1029/2003JB002756.

Fukahata, Y., and T. J. Wright (2008), A non-linear geodetic data inversion using ABIC for slip distribution on a fault with an unknown dip angle, *Geophys. J. Int.*, *173*(2), 353–364, doi:10.1111/j.1365-246X.2007.03713.x.

Fukuda, J. I., and K. M. Johnson (2008), A fully Bayesian inversion for spatial distribution of fault slip with objective smoothing, *Bull. Seismol. Soc. Am.*, *98*(3), 1128–1146, doi:10.1785/0120070194.

Fukuda, J. i., and K. M. Johnson (2010), Mixed linear-non-linear inversion of crustal deformation data: Bayesian inference of model, weighting and regularization parameters, *Geophys. J. Int.*, *181*(3), 1441–1458.

Hanks, T. C. (1977), Earthquake stress drops, ambient tectonic stresses and stresses that drive plate motions, *Pure Appl. Geophys.*, *115*(1–2), 441–458, doi:10.1007/BF01637120.

Harris, R., and P. Segall (1987), Detection of a locked zone at depth on the Parkfield, California, segment of the San Andreas Fault, *J. Geophys. Res.*, *92*(B8), 7945–7962, doi:10.1029/JB092iB08p07945.

Jonsson, S., H. Zebker, P. Segall, and F. Amelung (2002), Fault slip distribution of the 1999 M_w 7.1 Hector Mine, California, earthquake, estimated from satellite radar and GPS measurements, *Bull. Seismol. Soc. Am.*, *92*(4), 1377–1389, doi:10.1785/0120000922.

Keilis-Borok, V. I. (1957), On estimation of the displacement in an earthquake source and of source dimensions, *Ann. Geofis.*, *12*, 17–20.

Knopoff, L. (1958), Energy release in earthquakes, *Geophys. J. R. Astron. Soc.*, *1*, 44–52.

Matthews, M. V., and P. Segall (1993), Estimation of depth-dependent fault slip from measured surface deformation with application to the 1906 San Francisco earthquake, *J. Geophys. Res.*, *98*(B7), 12,153–12,163.

Okada, Y. (1992), Internal deformation due to shear and tensile faults in a half-space, *Bull. Seismol. Soc. Am.*, *82*(2), 1018–1040.

Ripperger, J., and P. M. Mai (2004), Fast computation of static stress changes on 2-D faults from final slip distributions, *Geophys. Res. Lett.*, *31*, L18610, doi:10.1029/2004GL020594.

Rosen, P. A., S. Henley, M. Simons, and G. Peltzer (2004), Updated repeat orbit interferometry package released, *Eos Trans. AGU*, *85*(5), 47, doi:10.1029/2004EO050004.

Scholz, C. H. (2002), *The Mechanics of Earthquakes and Faulting*, 2nd ed., 496 pp., Cambidge Univ. Press, New York.

Shaw, B. (2009), Constant stress drop from small to great earthquakes in magnitude-area scaling, *Bull. Seismol. Soc. Am.*, *99*(2A), 871–875, doi:10.1785/0120080006.

Shen, Z., J. Sun, P. Zhang, Y. Wan, M. Wang, R. Burgmann, Y. Zeng, W. Gan, H. Liao, and Q. Wang (2009), Slip maxima at fault junctions and rupturing of barriers during the 2008 Wenchuan earthquake, *Nat. Geosci.*, *2*(10), 718–724, doi:10.1038/ngeo636.

Sun, J., Z. Shen, X. Xu, and R. Bürgmann (2008), Synthetic normal faulting of the 9 January 2008 Nima (Tibet) earthquake from conventional and along-track SAR interferometry, *Geophys. Res. Lett.*, *35*, L22308, doi:10.1029/2008GL035691.

Talebian, M., et al. (2004), The 2003 Bam (Iran) earthquake: Rupture of a blind strike-slip fault, *Geophys. Res. Lett.*, *31*, L11611, doi:10.1029/2004GL020058.

Yabuki, T., and M. Matsu'ura (1992), Geodetic data inversion using a Bayesian information criterion for spatial distribution of fault slip, *Geophys. J. Int.*, *109*(2), 363–375, doi:10.1111/j.1365-246X.1992.tb00102.x.

Yun, S., P. Segall, and H. Zebker (2006), Constraints on magma chamber geometry at Sierra Negra Volcano, Galapagos Islands, based on InSAR observations, *J. Volcanol. Geotherm. Res.*, *150*(1–3), 232–243, doi:10.1016/j.jvolgeores.2005.07.009.

R. Bürgmann, Department of Earth and Planetary Science, University of California, Berkeley, 307 McCone Hall, Berkeley, CA 94720-4767, USA.

Z. Cao, Xizang Seismological Bureau, 22 Niangre Rd., Lhasa 850000, China.

K. M. Johnson, Department of Geological Sciences, Indiana University, 1001 East 10th St., Bloomington, IN 47405-1405, USA.

Z. Shen, Department of Geophysics, Peking University, Beijing 100871, China.

J. Sun, State Key Laboratory of Earthquake Dynamics, Institute of Geology, China Earthquake Administration, PO Box 9803, Beijing 100029, China. (sunjianbao@gmail.com)

X. Xu, Institute of Geology, China Earthquake Administration, Dewai, Quijiahuozi, Beijing 100029, China.